Few-photon single ionization of cold rubidium in the over-the-barrier regime

Huanyu Ma,[1,2,3] Xincheng Wang,[1,*] Linxuan Zhang,[4,5] Zhihan Zou,[1,2,3] Junyang Yuan,[1,2,3] Yixuan Ma,[1,2,3] Rujin Lv,[2,3] Zhenjie Shen,[2] Tianmin Yan,[2] Matthias Weidemüller,[6] Difa Ye,[4,†] and Yuhai Jiang[1,2,3,‡]

[1]*Center for Transformative Science and School of Physical Science and Technology, ShanghaiTech University, Shanghai 201210, China*
[2]*Shanghai Advanced Research Institute, Chinese Academy of Sciences, Shanghai 201210, China*
[3]*School of Future Technology, University of Chinese Academy of Sciences, Beijing 100049, China*
[4]*Laboratory of Computational Physics, Institute of Applied Physics and Computational Mathematics, Beijing 100088, China*
[5]*Graduate School, China Academy of Engineering Physics, Beijing 100193, China*
[6]*Physikalisches Institut, Universität Heidelberg, Im Neuenheimer Feld 226, 69120 Heidelberg, Germany*

(Received 15 November 2022; revised 2 February 2023; accepted 10 March 2023; published 20 March 2023)

Photoionization of rubidium atoms cooled in a magneto-optical trap, characterized by the coexistence of the ground $5S_{1/2}$ and excited $5P_{3/2}$ states, is investigated experimentally and theoretically with the 400-nm femtosecond laser pulses at intensities of $I = (3 \times 10^9)$–(4.5×10^{12}) W/cm^2. The recoil-ion momentum distribution (RIMD) of Rb^+ exhibits rich ringlike structures and their energies correspond to one-photon ionization of the $5P_{3/2}$ state and two-photon and three-photon ionizations of the $5S_{1/2}$ state, respectively. With increasing I, the dips near zero momentum (NZM) in the experimental RIMDs become shallow dramatically and their peaked Rb^+ momenta ionized from the $5P_{3/2}$ state move obviously toward zero while the peaks from the $5S_{1/2}$ state do not shift. In addition, the ion-yield ratio of the $5S_{1/2}$ state to the $5P_{3/2}$ state varies from I to $I^{1.5}$ as I increases. These features indicate a transition from perturbative ionization to strongly perturbative ionization for the $5P_{3/2}$ state. Numerical simulations by solving the time-dependent Schrödinger equation (TDSE) can qualitatively explain the measurements of the RIMD, photoion angular distributions, and ion-yield ratio. However, some discrepancies still exist, especially for the NZM dip, which could stem from the electron-electron correlation that is neglected in the present TDSE simulations since we have adopted the single-active-electron approximation.

DOI: 10.1103/PhysRevA.107.033114

I. INTRODUCTION

The study of the ionization of materials in various light sources can be traced back to the photoelectric effect, which is the most elementary process in light-matter interactions [1,2]. With the development of the ultrashort superintense laser, a series of novel nonlinear phenomena such as multiphoton ionization (MPI), tunneling ionization, and over-the-barrier ionization was revealed [3]. These different ionization mechanisms are clearly distinguished via the Keldysh parameter $\gamma = \sqrt{I_p/2U_p}$ [4], where I_p is the ionization energy of an atom, $U_p = 2\pi I/c\omega^2$ is the average quiver energy of an electron in a laser field with intensity I and frequency ω, and c is the speed of light in vacuum in atomic units. When the laser intensity is low or the laser frequency is high, for $\gamma \gg 1$, photoionization is considered to be a perturbative process described by the absorption of multiple photons [5]. In this perturbative MPI regime, the ionization rate depends on the laser intensities according to a power law $\mathcal{Y} \sim I^n$, with n the number of photons absorbed [6]. Photoelectron spectra can show a series of equally spaced sharp peaks separated by one-photon energy and these peaks are called above-threshold ionization (ATI) [7,8]. The spectral strength of ATI decreases rapidly with the number of absorbed photons. As I increases, the strength of the ATI peaks no longer follows $\mathcal{Y} \sim I^n$ and the position of ATI is shifted to the lower kinetic energy by $E_k(n) = n\hbar\omega - I_p - U_p$, where the effect of U_p becomes visible, resulting in a strongly perturbative MPI phenomenon [9,10]. As I increases continually, the ionization mechanism of the electrons will become tunneling ionization [11–13], in which the laser field distorts the atomic potential to form a potential barrier through which the electron can tunnel. In this case, $\gamma \ll 1$ and the energy spectrum is much smoother than that of MPI. At $I_{\mathrm{OBI}} = c\mathcal{E}_{\mathrm{OBI}}^2/8\pi$, with $\mathcal{E}_{\mathrm{OBI}} = I_p^2/4Z$ (Z is the charge number of the ion) [14,15], the barrier formed by the Coulomb potential and the laser field is completely suppressed and the electrons can classically escape via the over-the-barrier ionization (OBI). In general, the aforementioned ionization pictures categorized by the values of γ and $\mathcal{E}_{\mathrm{OBI}}$ work quite well for noble gases, where MPI and OBI occur at low and high laser intensities, respectively, and tunneling ionization appears in between [16].

Turning to the alkali-metal atoms, I_{OBI} is relatively small due to its lower ionization threshold in comparison with noble gases and its corresponding Keldysh parameter is far larger than 1, which leads to the overlapping of the MPI and OBI regimes. Analysis has shown that when the laser intensity exceeds the OBI threshold, due to strong depletion of the ground state, most atoms can be ionized before reaching the peak intensity of the laser [17,18]. In the literature, sustained MPI beyond the OBI was previously measured in lithium atoms

*wangxch1@shanghaitech.edu.cn
†ye_difa@iapcm.ac.cn
‡jiangyh3@shanghaitech.edu.cn

and sodium atoms and studied theoretically in potassium atoms [19–22]. Later Wessels *et al.* [23] measured strong-field ionization probabilities of ultracold Rb atoms and concluded that MPI remains a dominating mechanism even when $I > I_{\mathrm{OBI}}$. So far, most of the experimental and theoretical studies for alkali-metal atoms focused on the ionization mechanisms of the ground state with various photon wavelengths [17–23].

For Rb atoms cooled in a magneto-optical trap (MOT), as are of concern in this article, there is natural coexistence of the ground $5S_{1/2}$ and the excited $5P_{3/2}$ states. In the present mixture regime of MPI and OBI, ionization mechanisms will behave differently along with the change of laser intensities because of the different ionization energies of the $5S_{1/2}$ and $5P_{3/2}$ states, which might manifest in the variation of the ionization probabilities and the associated recoil-ion momentum distributions (RIMDs) as a function of laser intensity. In addition, photoion angular distributions (PADs), another particularly sensitive observable, can provide an additional view of the underlying mechanisms involved in photoionization and their related properties, such as information on continuous states and interchannel coupling [24–26].

In this paper we apply a 400-nm linearly polarized femtosecond laser to study the single ionization of cold rubidium atoms created with a MOT. We investigate the ion yield and the RIMDs of Rb^+ at laser intensities of $I = (3 \times 10^9)$–(4.5×10^{12}) W/cm^2 penetrating across the OBI region from the MPI regime. The magneto-optical trap recoil-ion momentum spectroscopy (MOTRIMS) [27–32], combining cold atoms, a strong laser pulse, and ultrafast technologies, was employed to detect Rb^+, in which the rubidium targets are cooled down to hundreds of μK to achieve high-resolution recoil-ion spectroscopy [33]. Owing to the laser wavelength that we have chosen, different ionization pathways resulting from the Rb($5S_{1/2}$) and Rb($5P_{3/2}$) states are well separated in the RIMDs as concentric rings. It delivers possibilities for comparative studies of the different ionization mechanisms of Rb($5S_{1/2}$) and Rb($5P_{3/2}$) for the same laser parameters. As we will show, the relative strength of these few- (one-, two-, or three-) photon ionization (FPI) rings can be used to determine the population ratio of the excited state to the ground state and as an indication of the onset of strongly perturbative FPI. Moreover, the PAD of each ring can be also extracted, which provides quantitative information on the dominant partial waves linking to the so-called asymmetry parameters of the PAD. Finally, we discuss the remaining differences between the experiment and present simulations. Our benchmark measurements can serve as a stringent testing ground for the further development of theory.

The paper is organized as follows. The experimental devices and theoretical simulation methods are introduced in Secs. II and III, respectively. The results are demonstrated and discussed in detail in Sec. IV. The paper ends with a summary in Sec. V. Atomic units are used throughout the paper unless otherwise specified.

II. EXPERIMENT

A schematic diagram of the experimental devices, the MOTRIMS, is shown in Fig. 1(a). Since the details of this setup can be found in Ref. [33], only a brief description is

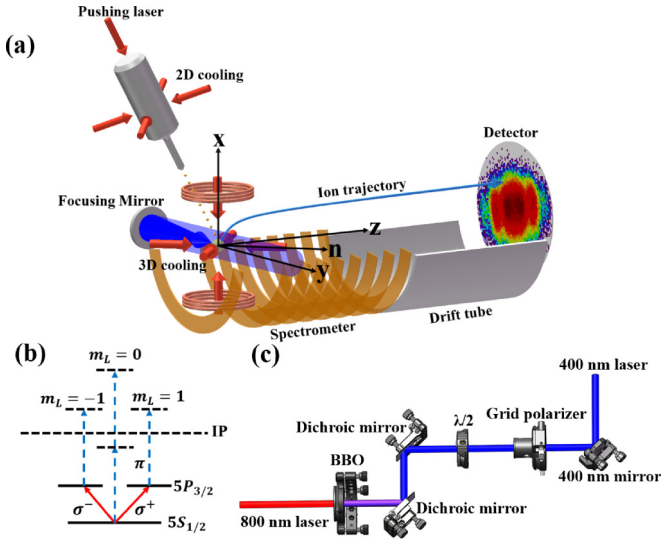

FIG. 1. (a) Schematic diagram of the MOTRIMS device. The Rb atoms are precooled in a 2D MOT and then pushed by a red-detuned pushing laser into the main experimental chamber, where they are cooled again by the 3D MOT and trapped in the center of the cavity, at last, ionized by a 400-nm femtosecond laser. The red arrows represent the 780-nm cooling lasers and the blue arrow represents the 400-nm femtosecond laser focused by the spherical on-axis concave mirror. We define the polarization direction of the femtosecond laser as z and its propagation direction as y. There are six cooling laser beams: two in the x axis and four in the yz plane spanning an angle of 45° to the z axis. (b) Diagram of the energy levels of the Rb atom. The red arrows represent the 780-nm cooling laser, which prepares the Rb atom in the excited state, and the blue dashed arrows represent the 400-nm ionizing femtosecond laser. (c) Layout of the beamline for the generation of a 400-nm femtosecond laser pulse. The colors red, purple, and blue represent an 800-nm seed laser beam, the 400- and 800-nm cobeam, and the 400-nm final output laser beam, respectively.

presented here. An intense femtosecond laser is focused on the target by a spherical mirror with a focal length of about 75 mm. The recoil ions are accelerated by a uniform electric field (approximately 0.5 V/cm) and then guided through a field-free drift region. The lengths of the acceleration and drift regions are 12 and 68 cm, respectively. The arriving time and impact position of the ions are measured by a time- and position-sensitive detector and a microchannel plate chevron stack with a delay-line anode, to reconstruct the initial momentum vectors.

The cold atoms used in this work originate from Rb vapor, which is precooled by a two-dimensional (2D) MOT in a glass cavity with ultrahigh vacuum. A red-detuned light is used to push these precooled atoms to the main experimental chamber, where they can be recaptured and further cooled by a 3D MOT. It should be noted that the cold Rb targets can be prepared in three different ways in the reaction regime. With the 3D MOT cooling lasers and gradient magnetic field on, it is depicted as a 3D MOT target, while by switching off the magnetic field, the molasses target can be prepared. Furthermore, the direct Rb beam from the 2D MOT, which has the lowest density, can also be used without further

cooling; this is referred as the 2D MOT target. In this work we adopt the molasses target when $I < 10^{10}$ W/cm^2 and the 2D MOT target when $I > 10^{10}$ W/cm^2. The reason is that the molasses target density is one order of magnitude higher than that of the 2D MOT target. So the molasses target can guarantee a faster count rate. However, it might suffer space charge effects when the laser intensity is high [34]; in this case, we choose the 2D MOT target instead. With the 780-nm circularly polarized cooling lasers used in the 2D and 3D MOTs, the Rb atoms can be excited from the ground state ($5S_{1/2}$) to the $5P_{3/2}$ state. The energy levels of the Rb atom are shown in Fig. 1(b). The population of the ground state is estimated to be several times higher than the excited state for all three targets, depending on the intensity and detuning of the cooling laser [35–38]. It should be noted that, since the temperatures of these three targets are all on the order of 100 μK, the influence of thermal motion on the recoil-ion momentum can be neglected.

The laser pulse used in the experiment is produced by a Ti:sapphire femtosecond laser operating at 1 KHz, with a central wavelength of 800 nm and pulse duration [full width at half maximum (FWHM)] of 35 fs. As shown in Fig. 1(c), a 200-μm-thick β barium borate octave crystal generates the second harmonic (400 nm) of the fundamental frequency laser (800 nm) with conversion efficiency as high as approximately 30%. With two dichroic mirrors (98% reflectance at 400 nm and 99% transmittance at 800 nm), a pure 400-nm laser can be obtained, which is used to ionize the Rb target in the reaction chamber. The corresponding bandwidth measured by the optical fiber spectrometer is 3.5 nm, which does not cover the 5*S*-6*P* resonance at 420 nm. The intensity of the beam is controlled by the $\lambda/2$ waveplate in front of a grid polarizer. In this work the laser peak intensities are estimated to be $I = (3 \times 10^9)$–(4.5×10^{12}) W/cm^2. The laser intensity is calculated from the repetition rate (1 KHz), pulse duration (35 fs), beam waist radius (39 μm), and power (10 μW to 15 mW). The uncertainty of the peak intensity is estimated to be ±50% [39]. It should be noted that the grid polarizer ensures a stable linear polarization along the horizontal direction.

III. THEORETICAL METHOD

Theoretically, the system is described by the time-dependent Schrödinger equation (TDSE) in the length gauge and under the dipole approximation

$$i\frac{\partial\Psi(\mathbf{r},t)}{\partial t} = \left[-\frac{1}{2}\nabla^2 + V_0(r) + V(\mathbf{r},t)\right]\Psi(\mathbf{r},t). \quad (1)$$

Here $V_0(r)$ is the effective atomic potential of Rb [40] and $V(\mathbf{r},t)$ stands for the atom-field interaction

$$V_0(r) = -\frac{1+(Z-1)e^{-a_1 r} + a_2 r e^{-a_3 r}}{r}, \quad (2)$$

$$V(\mathbf{r},t) = \mathcal{E}(t) r\cos\theta, \quad (3)$$

where $\mathbf{r}$ is the position of the electron with respect to the nucleus, θ is the angle between $\mathbf{r}$ and the polarization direction (z axis) of the laser electric field, and the atomic parameters are $Z = 37$, $a_1 = 3.431$, $a_2 = 10.098$, and $a_3 = 1.611$. The external electric field $\mathcal{E}(t)$ takes the form

$$\mathcal{E}(t) = \mathcal{E}_0 \sin^2\left(\frac{\pi t}{2\tau}\right)\cos(\omega t), \quad (4)$$

in which $\mathcal{E}_0$ represents the electric-field amplitude and τ is the pulse duration defined as the FWHM. The TDSE is solved through the generalized pseudospectral technique in the spherical coordinates [41,42]. Then, to get the momentum-resolved ionization probability, we expand the final wave function in the momentum-normalized Coulomb wave functions [43]

$$\Psi_{\mathbf{p}}^{C}(\mathbf{r}) = \sum_{lm}\sqrt{\frac{2}{\pi}} i^l e^{-i(\delta_l+\triangle_l)}\frac{R_{pl}(r)}{pr} Y_{lm}^*(\hat{\mathbf{p}})Y_{lm}(\hat{\mathbf{r}}), \quad (5)$$

with l the orbital quantum number, m the magnetic quantum number, δ_l the phase shift caused by the short-range distortion of the asymptotic Coulomb field, $\triangle_l$ the Coulomb phase shift, Y_{lm} the spherical harmonics, and R_{pl} the reduced radial function that satisfies the equation

$$-\frac{1}{2}\frac{d^2R_{pl}}{dr^2} + \left[\frac{l(l+1)}{2r^2} + V_0(r)\right]R_{pl} = \frac{1}{2}p^2 R_{pl}. \quad (6)$$

The momentum distribution of the photoelectron is then determined by

$$f(\mathbf{p}) = \left|\sum_{lm}\frac{1}{p}\sqrt{\frac{2}{\pi}} i^{-l} e^{i(\delta_l+\triangle_l)} Y_{lm}(\hat{\mathbf{p}})\int_0^\infty R_{pl}(r)\chi_{lm}(r)dr\right|^2, \quad (7)$$

in which $\chi_{lm}(r)$ is the reduced radial function of the final wave function corresponding to the spherical harmonic Y_{lm}.

In our simulations, the time evolutions starting from the ground state and the excited state need to be traced separately and then the final momentum distributions should be summed together incoherently. For convenience and without loss of generality, we assume that the femtosecond laser propagates along the y axis, with its electric field polarizing in the z direction, as shown in Fig. 1(a). Meanwhile, there exist six beams of cooling laser which will excite and polarize the electrons in different directions, i.e., along the cooling laser beam directions n_1, n_2, n_3, n_4, $n_5(+x)$, and $n_6(-x)$, with a magnetic quantum number $m = 1$. Therefore, the initial wave function of the excited electrons can be expressed as

$$\psi_{5P}^{n_i}(r,\theta,\varphi) = R_{5P}(r)Y_{11}^{n_i}(\theta,\varphi). \quad (8)$$

It should be noted that the polarization directions n_i ($i = 1, 2, \ldots, 6$) of the excited electrons are different from the main axis of the system that is previously chosen along the ionizing laser's polarization direction z. Thus it would be convenient to transform the spherical harmonic functions as follows:

$$Y_{11}^{x} = \frac{1}{2}Y_{11}^{z} + \frac{\sqrt{2}}{2}Y_{10}^{z} + \frac{1}{2}Y_{1-1}^{z}, \quad (9)$$

$$Y_{11}^{-x} = \frac{1}{2}Y_{11}^{z} - \frac{\sqrt{2}}{2}Y_{10}^{z} + \frac{1}{2}Y_{1-1}^{z}, \quad (10)$$

$$Y_{11}^{n_1} = \frac{2+\sqrt{2}}{4}Y_{11}^{z} + \frac{i}{2}Y_{10}^{z} - \frac{2-\sqrt{2}}{4}Y_{1-1}^{z}, \quad (11)$$

$$Y_{11}^{n_2} = \frac{2-\sqrt{2}}{4}Y_{11}^{z} + \frac{i}{2}Y_{10}^{z} - \frac{2+\sqrt{2}}{4}Y_{1-1}^{z}, \quad (12)$$

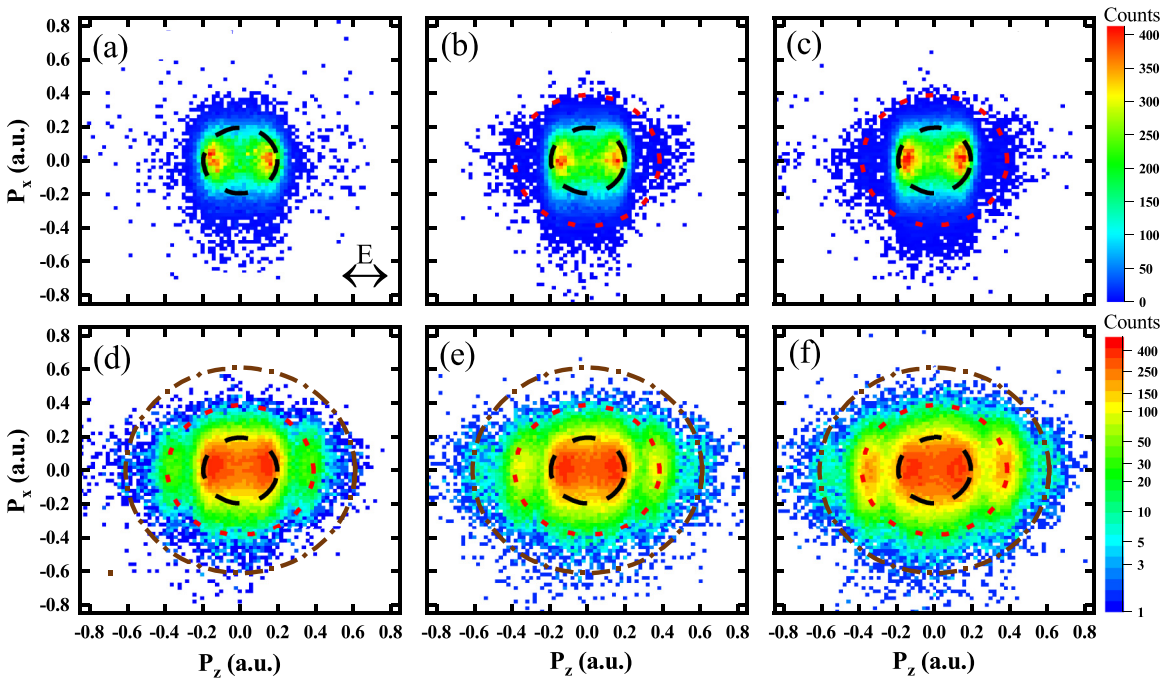

FIG. 2. The 2D RIMDs of Rb^+ ions obtained in the experiment, for which p_z and p_x represent the momenta parallel and perpendicular to the laser polarization direction, respectively. The double arrow indicates the laser polarization direction. The laser intensities are (a) $I = 3 \times 10^9$ W/cm^2, (b) $I = 1.5 \times 10^{11}$ W/cm^2, (c) $I = 3 \times 10^{11}$ W/cm^2, (d) $I = 1.5 \times 10^{12}$ W/cm^2, (e) $I = 3 \times 10^{12}$ W/cm^2, and (f) $I = 4.5 \times 10^{12}$ W/cm^2. The black dashed circles mark the theoretically expected recoil-ion momentum from single-photon ionization of the $5P_{3/2}$ state, while the red dotted circles and brown dash-dotted circles indicate the two-photon ionization and three-photon ionization of the $5S_{1/2}$ state, respectively.

$$Y_{11}^{n_3} = \frac{2-\sqrt{2}}{4} Y_{11}^z - \frac{i}{2} Y_{10}^z - \frac{2+\sqrt{2}}{4} Y_{1-1}^z, \tag{13}$$

$$Y_{11}^{n_4} = \frac{2+\sqrt{2}}{4} Y_{11}^z - \frac{i}{2} Y_{10}^z - \frac{2-\sqrt{2}}{4} Y_{1-1}^z. \tag{14}$$

Because the ionizing laser is linearly polarized, the quantum number m (with respect to the ionizing laser polarization direction) is conserved during the ionization process, which implies that the Y_{lm}^z $(m = 0, \pm 1)$ components can be propagated independently and the final momentum distribution should be summed over these components coherently according to the above transforming coefficients. This can save a great deal of computational time in comparison to directly solving the TDSE over the whole Hilbert space.

After solving the TDSE, the momentum distributions of the exited Rb atoms are averaged over the six polarization directions, i.e.,

$$f_{5P}(\mathbf{p}) = \tfrac{1}{6} \sum_{i=1}^{6} f_{5P,m=1}^{n_i}(\mathbf{p}), \tag{15}$$

where the subscripts $5P$ and $m = 1$ represent that the momentum distribution is calculated from the initial state with the orbital angular momentum $l = 1$ and the magnetic angular momentum $m = 1$ and the superscripts indicate the polarization directions. For the ground state ($|5S, m = 0\rangle$), there exists a spherical symmetry, so the direction of the main axis can be chosen arbitrarily, which implies that the ionization momentum distribution from the ground state can be expressed as

$$f_{5S}(\mathbf{p}) = f_{5S,m=0}^z(\mathbf{p}). \tag{16}$$

Finally, the momentum distributions of the ground state and the excited state should be added together

$$f(\mathbf{p}) = \frac{1}{1+\alpha} f_{5P}(\mathbf{p}) + \frac{\alpha}{1+\alpha} f_{5S}(\mathbf{p}), \tag{17}$$

where α is the population ratio of the ground state to the excited state, which will be determined later by the best fitting between the experimental and theoretical RIMDs.

IV. RESULTS AND DISCUSSION

As described above, the Keldysh parameter γ can be used as an indication of whether a tunneling picture or multiphoton ionization picture should be considered. The laser intensities in this work range from 3×10^9 to 4.5×10^{12} W/cm^2, which correspond to γ values between 215.7 (169.66) and 5.57 (4.38) for the $5S_{1/2}$ ($5P_{3/2}$) state. This allows us to consider the ionization of Rb atoms as a few-photon ionization process. It is worth noting that a certain range of the laser intensities in this work has surpassed the OBI threshold, i.e., $I_c = 1.2 \times 10^{12}$ W/cm^2 ($5S_{1/2}$ state) and 1.77×10^{11} W/cm^2 ($5P_{3/2}$ state); the ionization should be considered as a strongly perturbative FPI process [19–22]. As indicated by the vertical blue arrows in Fig. 1(b), the Rb atoms in the $5S_{1/2}$ state are mainly ionized through two-photon ionization while those in the excited $5P_{3/2}$ state with different magnetic quantum numbers are mainly proceed through single-photon ionization.

Since the photon momentum is small and can be neglected, the recoil-ion momentum can be deduced from the photoelectron momentum according to the momentum conservation law as follows:

$$\mathrm{Rb}(5P) + \hbar\omega(3.1\ \mathrm{eV}) \rightarrow \mathrm{Rb}^+ + e(p_r = 0.2\ \mathrm{a.u.}), \quad (18)$$

$$\mathrm{Rb}(5S) + 2\hbar\omega(6.2\ \mathrm{eV}) \rightarrow \mathrm{Rb}^+ + e(p_r = 0.39\ \mathrm{a.u.}). \quad (19)$$

These relationships can be used as a guide to distinguish different pathways contributed by the $5S_{1/2}$ and $5P_{3/2}$ states to the momentum spectra.

The measured RIMDs in the polarization (x-z) plane of the ionizing laser are presented in Fig. 2. Here, to reduce the effect of diffraction associated with the laser spatial profile and its Rayleigh length, the data are extracted with a constraint of the momentum in the laser propagation direction, i.e., $|p_y| < 0.2$ a.u. [44,45]. When the laser intensity is as low as 3×10^9 W/cm^2 [Fig. 2(a)], a clear double-lobe structure can be observed in the region of -0.2 a.u. $< p_z < -0.1$ a.u. and -0.2 a.u. $< p_x < 0.2$ a.u. and the region of 0.1 a.u. $< p_z < 0.2$ a.u. and -0.2 a.u. $< p_x < 0.2$ a.u., pointing to the dominance of one-photon ionization of the excited state, as indicated by the black dashed circle with the theoretically predicted momentum $p_r = 0.2$ a.u. This can be understood since the photoionization cross section of the $5P_{3/2}$ state of Rb is much larger than that of the $5S_{1/2}$ state [38,46,47]. With the laser intensity increasing from 3×10^9 to 4.5×10^{12} W/cm^2, more structures can be observed at the higher-energy (momentum) part of the spectra. For example, the two-photon ionization of Rb from the $5S_{1/2}$ state, indicated by the red dashed circle with $p_r = 0.39$ a.u., appears at (1.5×10^{11})–(4.5×10^{12}) W/cm^2. The three-photon ATI of the $5S_{1/2}$ state is also detected, as marked by the brown dash-dotted ring at $p_r = 0.61$ a.u. in Figs. 2(d) and 2(e). These observations demonstrate the well-known fact that the ion yields of the MPI process increase nonlinearly with the increasing laser intensity. However, the ATI peaks of the $5P_{3/2}$ state (e.g., two-photon ionization, which would be expected to show up at 0.52 a.u. if it exists) are not discernible even at the highest laser intensity.

To achieve deeper insight into these experimental measurements, we then perform a series of TDSE simulations, the details of which have been described in Sec. II. In general, the experimental observations are qualitatively reproduced by our quantum simulations over the whole range of laser intensities. Here, without loss of generality, we first present the data at $I = 4.5 \times 10^{12}$ W/cm^2, as shown in Fig. 3(a). Two main differences between theory and experiment can be readily observed: (i) The ATI ring of the $5P_{3/2}$ state (the third ring, counting outward from the center, not observed in the experiment) can be clearly identified along with three other rings observed in the experiment and (ii) these rings are much thinner than the experimental observations. To further account for the discrepancy between experiment and theory, we then convolve the simulation results with a 3D Gaussian function to mimic the resolution of the experimental measurements. The result is shown in Fig. 3(b), which is in good agreement with the experimental observation at the same laser intensity [recall Fig. 2(f)]. In theory, the contributions of the ground state and the excited state to the final momentum distribution can be

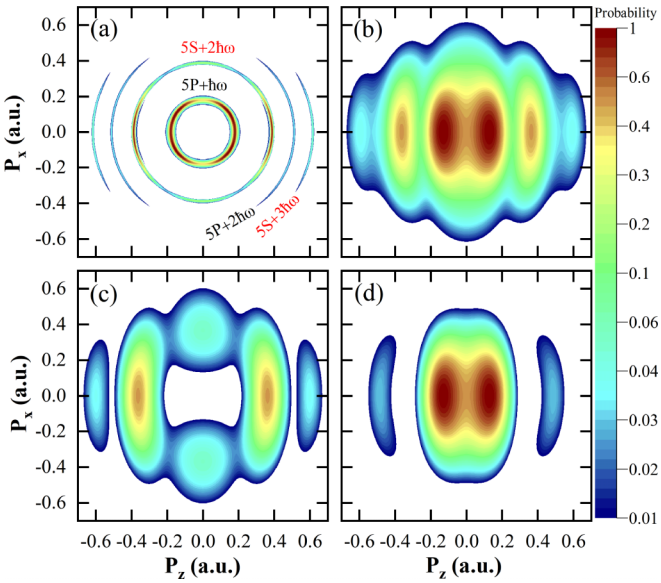

FIG. 3. The 2D RIMDs of Rb^+ from TDSE simulations at $I = 4.5 \times 10^{12}$ W/cm^2. The laser pulse FWHM is 35 fs, the same as that used in the experiment. (a) Raw data at $p_y = 0$ and (b) convolution of the simulation results and the resolution of the momentum measurements in the experiment, i.e., $\Delta p_z = 0.1$ a.u. and $\Delta p_x = \Delta p_y = 0.3$ a.u., then integrated over -0.2 a.u. $< p_y < 0.2$ a.u., as has been done in the experiment. The contributions of the (c) ground and (d) excited states are separated.

separated, as demonstrated in Figs. 3(c) and 3(d). These results explain why the ATI signature of the $5P_{3/2}$ state is barely observed in experiment since the signal is much weaker than that of the $5S_{1/2}$ state and, furthermore, the two-photon ATI of the $5P_{3/2}$ state and the two-photon ionization of the $5S_{1/2}$ state almost overlap in the momentum space due to the limited resolution of the experiment. Despite this, the main FPI structures are retained in the convolved momentum spectra (see also Fig. 4 for a more complete simulation at different laser intensities), which permits a quantitative comparison between experiments and theories, as will be shown in the following.

First, the RIMDs provide a means of determining the population ratio α of Rb in the $5S_{1/2}$ state to the $5P_{3/2}$ state. Experimentally, α is determined by the cooling laser intensity and detuning [35–38]. In order to get a quantitative estimation of α, we can take full advantage of the relative ion yields from the $5S_{1/2}$ state and the $5P_{3/2}$ state, represented by the ion counts (local maximum η_{5S} and η_{5P}) at the two bright spots around the two main FPI rings shown in Figs. 2 and 3. The ratio of the ion yields η_{5S}/η_{5P} is presented in Fig. 5 as a function of ionizing laser intensity for the experimental data (black closed circles) and the TDSE simulations (green triangles). Then α is treated as a parameter to be fitted with the least-squares method by comparing these two sets of results, and the best fitting between experiment and theory gives $\alpha = 3.85$. We can retrieve the relative ionization probability (RIP) between the two-photon ionization of the ground state and the one-photon ionization of the excited state from the RIMDs if the proportion of the excited states is *a priori* known from the MOT data (see, e.g., Ref. [38]). On the basis of the approximately 20% population of the

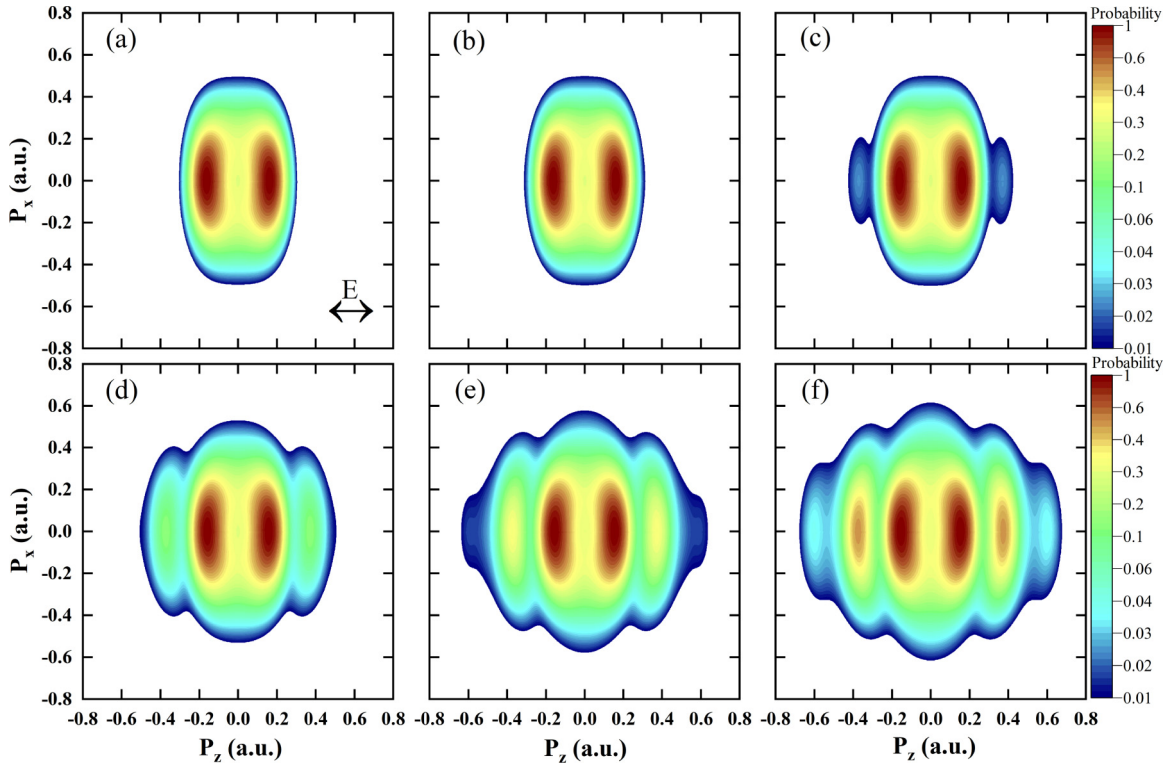

FIG. 4. Simulated 2D RIMDs of Rb^+ at six different laser intensities corresponding to the experimental measurements: (a) $I = 3 \times 10^9$ W/cm^2, (b) $I = 1.5 \times 10^{11}$ W/cm^2, (c) $I = 3 \times 10^{11}$ W/cm^2, (d) $I = 1.5 \times 10^{12}$ W/cm^2, (e) $I = 3 \times 10^{12}$ W/cm^2, and (f) $I = 4.5 \times 10^{12}$ W/cm^2. The spectra are obtained in the same way as in Fig. 3(b).

excited state extracted before, the RIPs are then determined from the experimental measurements as 0.003, 0.006, 0.025, 0.067, and 0.128 at laser intensities of 1.5×10^{11}, 3×10^{11}, 1.5×10^{12}, 3×10^{12}, and 4.5×10^{12} W/cm^2, respectively. We also note that the intensity-dependent scaling law of η_{5S}/η_{5P} can serve as an indication of the onset of strongly perturbative FPI. At lower laser intensities, according to the perturbation picture, the ion-yield ratio is expected to show a slope of 1 in this double logarithmic plot (see the red dashed line in Fig. 5), while for higher laser intensities, our TDSE calculation predicts a slope of about 1.5, as indicated by the black dashed line. The experimental results are in good agreement with these asymptotic predictions. The transition of the scaling law from I to $I^{1.5}$ as I increases is closely related to the ionization saturation of the excited state and therefore the ionization process should be considered as strongly perturbative FPI.

Second, the PAD is another sensitive probe of strong-field atomic ionization. By integrating the data over specific momentum intervals from the 2D RIMDs, the angular distribution of the recoil ion (equivalent to the corresponding PAD as a result of momentum conservation) originated from the $5S_{1/2}$ state and the $5P_{3/2}$ state can be extracted separately. At $I = 3 \times 10^9$ W/cm^2, the spectrum is dominated by one-photon ionization of the $5P_{3/2}$ state. Therefore, the PAD has a peanut shape [see Fig. 6(a)] with two main peaks at $\theta = 0^\circ$ and 180°, parallel to the laser polarization direction, pointing to the dominant d-wave ($|l = 2, m = 1\rangle_{n_i}$) emission according to the selection rule of dipole transitions. The result can be well fitted by the high-order Legendre polynomials

$$\frac{d\sigma}{d\Omega} = \frac{\sigma_0}{4\pi} \sum_{i=0}^{n} \beta_{2i} P_{2i}(\cos\theta), \tag{20}$$

where σ_0 is the total photoionization cross section, θ is the angle between the photoelectron momentum vector and the polarization vector of the laser, β is the anisotropy parameter, and P_{2i} are the Legendre polynomials in variable $\cos\theta$. The fitting value of the anisotropy parameter is $\beta_2 = 0.69$, in good agreement with the value reported in Ref. [48] (see Fig. 5 therein) utilizing the configuration-interaction Pauli-Fock method including core polarization potential but significantly deviating from the configuration-interaction Pauli-Fock calculation. This pinpoints the pivotal role of the core polarization effect on the outermost electron dynamics. With the increase of the laser intensity, the $5S_{1/2}$ state two-photon ionization gets more and more prominent. As shown in Fig. 6(b), the corresponding PAD shows not only two main peaks at $\theta = 0^\circ$ and 180° but also two side lobes in the perpendicular direction, with the fitting parameters $\beta_2 = 0.84$ and $\beta_4 = 1.13$. The PAD is formed by a superposition of the d wave ($|l = 2, m = 0\rangle$) and s wave ($|l = 0, m = 0\rangle$). The blue curves show the TDSE simulations for comparison, which are quantitatively consistent with the experimental measurements. The present results show that the MOTRIMS can obtain high-resolution and high-quality data to provide insights into detailed structures of the final momentum spectra.

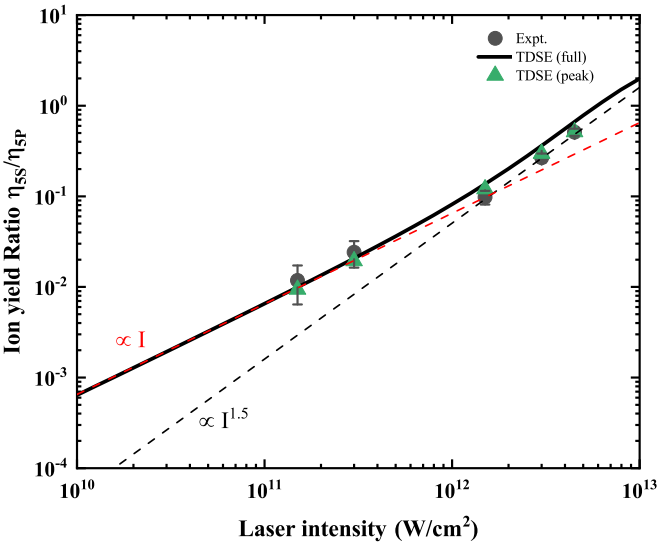

FIG. 5. The Rb^+ ion-yield ratio of the $5S_{1/2}$ state two-photon ionization to the $5P_{3/2}$ state single-photon ionization. The black solid curve is the full theoretical predictions, i.e., the total ion yield after integrating over the whole momentum space, while the scatters are estimations based on the bright spots on RIMDs for the experimental data (black closed circles) and the corresponding simulations (green triangles) (see the text for details). The best fitting between theory and experiment indicates that the population ratio of the $5S_{1/2}$ state to the $5P_{3/2}$ state is approximately 4:1. The red and black dashed lines are used to guide the eyes and demonstrate a transition of the scaling law from I, as predicted by a perturbative theory in the weak-field limit, to $I^{1.5}$ with the increase of I.

Finally, by integrating over p_x one can obtain the momentum spectrum of Rb^+ in the polarization direction, as shown in Fig. 7(a). Here the peaks at $p_z = 0.15$, 0.37, and 0.6 a.u. correspond to the three FPI rings in Fig. 2, respectively. For comparison, Fig. 7(b) shows the results of the TDSE simulations, which are qualitatively consistent with the experimental measurements. However, it should be noted that when the laser intensity is above 3×10^{11} W/cm^2, the experimental results show that the peak at $p_z = 0.15$ a.u., corresponding to the single-photon ionization of the $5P_{3/2}$ state, moves toward momentum zero with increasing laser intensity, which might be caused by the influence of the ponderomotive energy U_p as indicated by $E_k(n) = n\hbar\omega - I_p - U_p$, while this peak shift is not so clearly seen in theory. One might also argue that there is a broadening of the peaks as well, accompanied by their movement toward the zero. However, we cannot see definitive evidence for such a broadening from the present experimental spectra, since the movement of the peaks itself can already make the overlapping region seem broader. Another apparent difference between the experiment and theory can be observed at the NZM dip: Experimentally, the depth of the dip becomes much shallower as the laser intensity increases, but it seems to not vary significantly in the theoretical simulation. We try to further explain the discrepancy by adopting another set of model potentials that include more physical effects such as the spin-orbit coupling [49] and dynamical core polarization [50]. However, the results are almost identical to those shown in Fig. 7(b) and thus do not seem to solve the contradiction. We

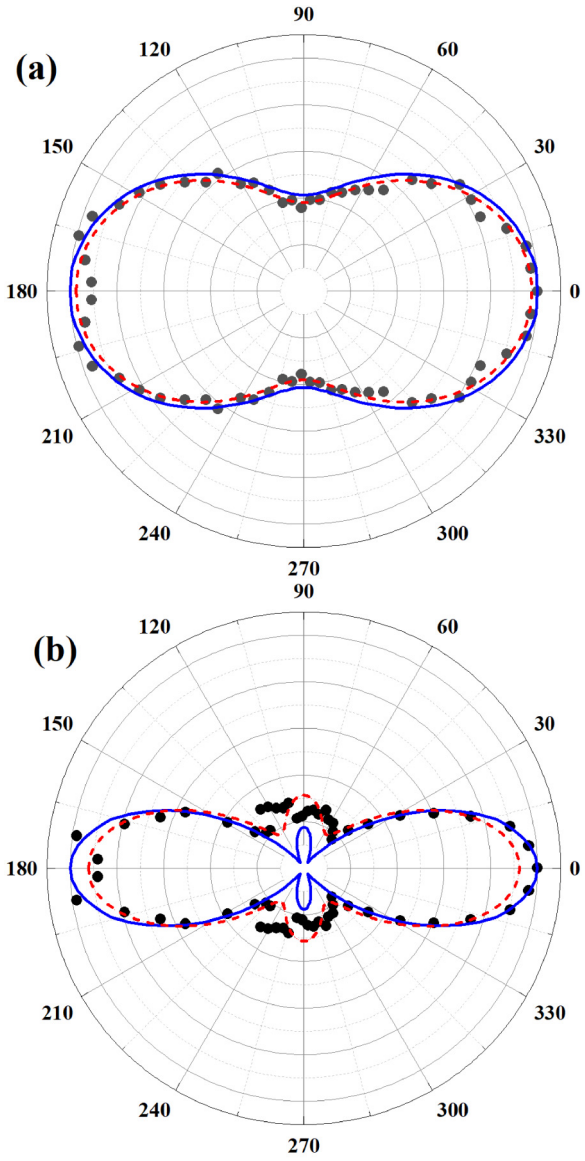

FIG. 6. Angular distributions of the Rb^+ ions for (a) single-photon ionization of the $5P_{3/2}$ state at $I = 3 \times 10^9$ W/cm^2 and (b) two-photon ionization of the $5S_{1/2}$ state at $I = 1.5 \times 10^{12}$ W/cm^2. The scatters are the experimental measurements. The red dashed curves are fitting results of the experimental data with the Legendre polynomials, while the blue solid curves are the corresponding theoretical predictions.

also would like to mention that, in our theoretical simulations, we did not consider the focal volume averaging effect because, as can be seen from Fig. 7, the central minimum is almost the same at different laser intensities (spanning three orders of magnitude), so the volume average will not change the depth of the NZM dip and thus is not helpful in explaining the filling of the central minimum observed in the experiment. Based on the above considerations, we therefore speculate that the remaining discrepancy could be induced by the dynamical electron-electron interaction that has been totally neglected in our TDSE simulations since we have adopted the single-active-electron approximation. This would be an interesting issue for further study.

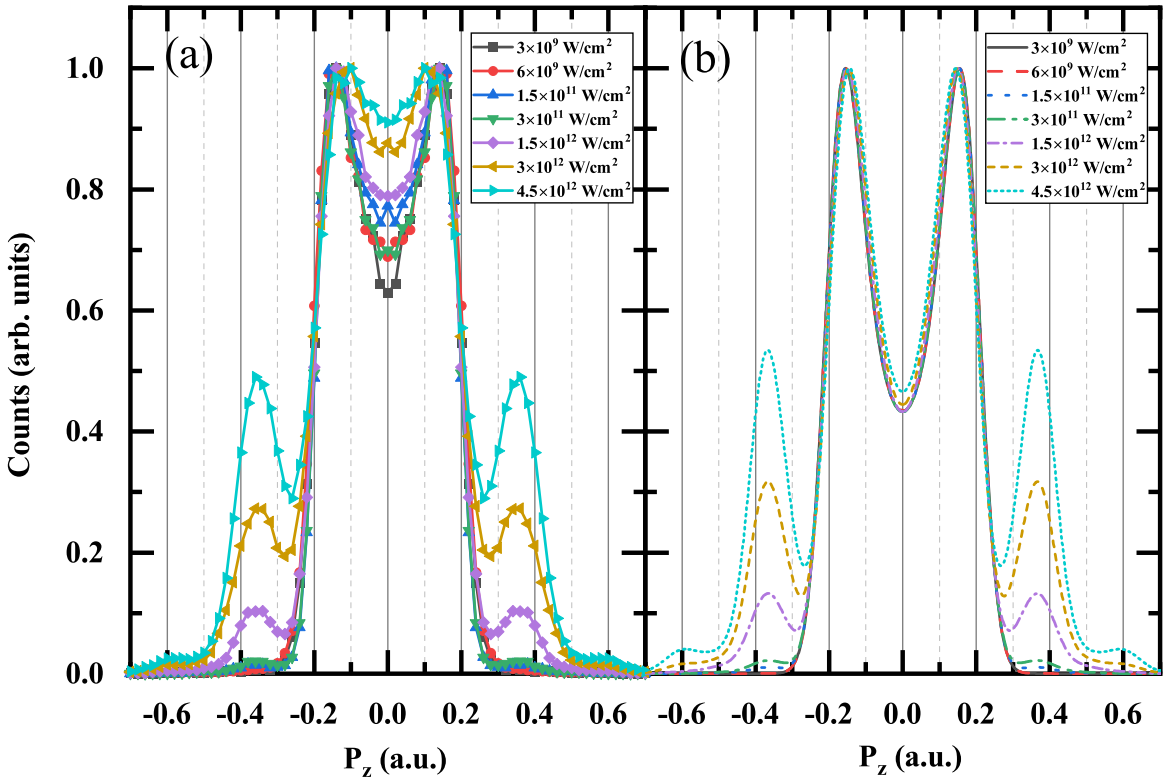

FIG. 7. Comparison of the (a) experimental and (b) theoretical momentum distributions of the Rb^+ ions in the laser polarization direction. The corresponding laser intensities are indicated in the legends in the figure. Each curve is normalized independently at the peak.

V. SUMMARY

With MOTRIMS technology and TDSE simulation, we have investigated the single ionization of cold rubidium atoms with 400-nm femtosecond laser pulses, where ionization processes of the ground state $5S_{1/2}$ and the excited state $5P_{3/2}$ are dominated by absorption of one, two, or three photons. Experimental and theoretical momentum spectra, ion yields, and angular distributions were studied as a function of laser intensities from $I = 3 \times 10^9$ to 4.5×10^{12} W/cm^2. With increasing I, we found that experimental NZM signals in the RIMDs resulting from the $5P_{3/2}$ state were enhanced dramatically and its peaked Rb^+ momenta moved toward zero obviously, while that from the $5S_{1/2}$ state did not shift. Meanwhile, the ion-yield ratio of the $5S_{1/2}$ state to the $5P_{3/2}$ state varies from I to $I^{1.5}$ as I increases, where the ionization yield of $5S_{1/2}$ state displays the intensity dependence of I^2 resulting from the two-photon absorption. These features indicate a completely perturbative two-photon ionization of the $5S_{1/2}$ state and a transition from perturbative one-photon ionization to strongly perturbative one-photon ionization of the $5P_{3/2}$ state. The TDSE simulation reproduces the feature in the ion-yield curve, and the simulated two-dimensional momentum distribution and angular distribution are also in good agreement with the experiment. This not only proves that the magneto-optical trap recoil-ion momentum spectrometer can obtain high-resolution and high-quality data, providing insights into the detailed structure of the final momentum space, but also verifies the reliability of the simulation method using the TDSE. However, there still exists some difference between the experimental results and theoretical simulations in the change of the NZM dip of the one-dimensional momentum distribution with the laser intensity, indicating that there are still some details to be considered for the accurate calculation of the process. The reasons for the differences remain to be explored in the future. We hope that the work presented here will inspire further studies for few-photon-induced ionization processes of alkali-metal atoms in the strong femtosecond laser field, both experimentally and theoretically.

ACKNOWLEDGMENTS

This work was supported by the National Key Research and Development Program of China (Grant No. 2022YFA1604302) and the National Natural Science Foundation of China (Grants No. 11827806 and No. 12174034).

[1] A. Einstein, Ann. Phys. (Leipzig) **322**, 132 (1905).
[2] A. A. Sorokin, S. V. Bobashev, T. Feigl, K. Tiedtke, H. Wabnitz, and M. Richter, Phys. Rev. Lett. **99**, 213002 (2007).
[3] M. Protopapas, C. H. Keitel, and P. L. Knight, Rep. Prog. Phys. **60**, 389 (1997).
[4] L. V. Keldysh, Sov. Phys. JETP **20**, 1307 (1965).

[5] G. S. Voronov, G. A. Delone, and N. B. Delone, JETP Lett. **1**, 66 (1966).

[6] F. Fabre, G. Petite, P. Agostini, and M. Clement, J. Phys. B **15**, 1353 (1982).

[7] P. Agostini, F. Fabre, G. Mainfray, G. Petite, and N. K. Rahman, Phys. Rev. Lett. **42**, 1127 (1979).

[8] Y. Gontier, M. Poirier, and M. Trahin, J. Phys. B **13**, 1381 (1980).

[9] R. R. Freeman, P. H. Bucksbaum, H. Milchberg, S. Darack, D. Schumacher, and M. E. Geusic, Phys. Rev. Lett. **59**, 1092 (1987).

[10] G. Petite, P. Agostini, and H. Muller, J. Phys. B **21**, 4097 (1988).

[11] M. V. Ammosov, N. B. Delone, and V. P. Krainov, Sov. Phys. JETP **64**, 1191 (1986).

[12] B. Walker, B. Sheehy, K. C. Kulander, and L. F. DiMauro, Phys. Rev. Lett. **77**, 5031 (1996).

[13] P. B. Corkum, N. H. Burnett, and F. Brunel, Phys. Rev. Lett. **62**, 1259 (1989).

[14] S. Augst, D. Strickland, D. D. Meyerhofer, S. L. Chin, and J. H. Eberly, Phys. Rev. Lett. **63**, 2212 (1989).

[15] S. Augst, D. D. Meyerhofer, D. Strickland, and S. L. Chin, J. Opt. Soc. Am. B **8**, 858 (1991).

[16] E. Mevel, P. Breger, R. Trainham, G. Petite, P. Agostini, A. Migus, J.-P. Chambaret, and A. Antonetti, Phys. Rev. Lett. **70**, 406 (1993).

[17] T. Morishita and C. D. Lin, Phys. Rev. A **87**, 063405 (2013).

[18] S.-D. Jheng and T. F. Jiang, J. Phys. B **46**, 115601 (2013).

[19] A. Bunjac, D. B. Popović, and N. S. Simonović, Phys. Lett. A **394**, 127197 (2021).

[20] M. Schuricke, G. Zhu, J. Steinmann, K. Simeonidis, I. Ivanov, A. Kheifets, A. N. Grum-Grzhimailo, K. Bartschat, A. Dorn, and J. Ullrich, Phys. Rev. A **83**, 023413 (2011).

[21] N. A. Hart, J. Strohaber, A. A. Kolomenskii, G. G. Paulus, D. Bauer, and H. A. Schuessler, Phys. Rev. A **93**, 063426 (2016).

[22] F. Morales, M. Richter, S. Patchkovskii, and O. Smirnova, Proc. Natl. Acad. Sci. USA **108**, 16906 (2011).

[23] P. Wessels, B. Ruff, T. Kroker, A. K. Kazansky, N. M. Kabachnik, K. Sengstock, M. Drescher, and J. Simonet, Commun. Phys. **1**, 32 (2018).

[24] Y. A. Klimova, S. I. Marmo, and A. V. Meremianin, Phys. Lett. A **377**, 1439 (2013).

[25] F. Thini, K. L. Romans, B. P. Acharya, A. H. N. C. de Silva, K. Compton, K. Foster, C. Rischbieter, O. Russ, S. Sharma, S. Dubey, and D. Fischer, J. Phys. B **53**, 095201 (2020).

[26] Y. Boran, N. Hart, N. Kaya, J. Zhou, A. A. Kolomenskii, and H. A. Schuessler, J. Phys. B **54**, 145401 (2021).

[27] R. Hubele, M. Schuricke, J. Goullon, H. Lindenblatt, N. Ferreira, A. Laforge, E. Bruehl, V. L. B. de Jesus, D. Globig, A. Kelkar, D. Misra, K. Schneider, M. Schulz, M. Sell, Z. Song, X. Wang, S. Zhang, and D. Fischer, Rev. Sci. Instrum. **86**, 033105 (2015).

[28] J. W. Turkstra, R. Hoekstra, S. Knoop, D. Meyer, R. Morgenstern, and R. E. Olson, Phys. Rev. Lett. **87**, 123202 (2001).

[29] H. Nguyen, X. Fléchard, R. Brédy, H. Camp, and B. DePaola, Rev. Sci. Instrum. **75**, 2638 (2004).

[30] S. Götz, B. Höeltkemeier, C. S. Hofmann, D. Litsch, B. D. DePaola, and M. Weidemüeller, Rev. Sci. Instrum. **83**, 073112 (2012).

[31] J. Yuan, S. Liu, X. Wang, Z. Shen, Y. Ma, H. Ma, Q. Meng, T.-M. Yan, Y. Zhang, A. Dorn, M. Weidemüller, D. Ye, and Y. Jiang, Phys. Rev. A **102**, 043112 (2020).

[32] J. Yuan, Y. Ma, R. Li, H. Ma, Y. Zhang, D. Ye, Z. Shen, T. Yan, X. Wang, M. Weidemüller, and Y. Jiang, Chinese Phys. Lett. **37**, 053201 (2020).

[33] R. Y. Li, J. Y. Yuan, X. C. Wang, X. Y. Hou, S. Zhang, Z. Y.Zhu, Y. X. Ma, Q. Gao, Z. Y. Wang, T. M. Yan, C. C. Qin, S. Li, Y. Z. Zhang, M. Weidermüller, and Y. H. Jiang, J. Instrum. **14**, P02022 (2019).

[34] G. Schönhense, K. Medjanik, C. Tusche, M. de Loos, B. van der Geer, M. Scholz, F. Hieke, N. Gerken, J. Kirschner, and W. Wurth, Ultramicroscopy **159**, 488 (2015).

[35] J. M. Kwolek, D. S. Goodman, S. A. Entner, J. E. Wells, F. A. Narducci, and W. W. Smith, Phys. Rev. A **97**, 053420 (2018).

[36] G. Veshapidze, J.-Y. Bang, C. W. Fehrenbach, H. Nguyen, and B. D. DePaola, Phys. Rev. A **91**, 053423 (2015).

[37] M. H. Shah, H. A. Camp, M. L. Trachy, G. Veshapidze, M. A. Gearba, and B. D. DePaola, Phys. Rev. A **75**, 053418 (2007).

[38] M. Witkowski, R. Munoz-Rodriguez, A. Raczyński, J. Zaremba, B. Nagórny, P. S. Żuchowski, R. Ciuryło, and M. Zawada, Phys. Rev. A **98**, 053444 (2018).

[39] A L'Huillier, L. A. Lompré, G. Mainfray, and C. Manus, J. Phys. B **16**, 1363 (1983).

[40] W. Schweizer, P. Faßbinder, and R. González-Férez, At. Data Nucl. Data Tables **72**, 33 (1999).

[41] X.-M. Tong and S.-I. Chu, Chem. Phys. **217**, 119 (1997).

[42] X. Wu, Z. Yang, S. Zhang, X. Ma, J. Liu, and D. Ye, Phys. Rev. A **103**, L061102 (2021).

[43] L. B. Madsen, L. A. A. Nikolopoulos, T. K. Kjeldsen, and J. Fernández, Phys. Rev. A **76**, 063407 (2007).

[44] W. A. Bryan, S. L. Stebbings, J. Mckenna, E. M. L. English, M. Suresh, J. Wood, B. Srigengan, I. C. E. Turcu, J. M. Smith, E. J. Divall, C. J. Hooker, A. J. Langley, J. L. Collier, I. D. Williams, and W. R. Newell, Nat. Phys. **2**, 379 (2006).

[45] W. A. Bryan, S. L. Stebbings, E. M. L. English, T. R. J. Goodworth, W. R. Newell, J. McKenna, M. Suresh, B. Srigengan, I. D. Williams, I. C. E. Turcu, J. M. Smith, E. J. Divall, C. J. Hooker, and A. J. Langley, Phys. Rev. A **73**, 013407 (2006).

[46] M. Anderlini, E. Courtade, D. Ciampini, J. Müller, O. Morsch, and E. Arimondo, J. Opt. Soc. Am. B **21**, 480 (2004).

[47] T. Takekoshi, G. M. Brooke, B. M. Patterson, and R. J. Knize, Phys. Rev. A **69**, 053411 (2004).

[48] I. D. Petrov, V. L. Sukhorukov, E. Leber, and H. Hotop, Eur. Phys. J. D **10**, 53 (2000).

[49] J. C. Weisheit, Phys. Rev. A **5**, 1621 (1972).

[50] Z. Zhao and T. Brabec, J. Mod. Opt. **54**, 981 (2007).